Journal of Materials Chemistry C

ROYAL SOCIETY OF CHEMISTRY

PAPER

View Article Online
View Journal | View Issue

Cite this: J. Mater. Chem. C, 2020, 8, 3784

Realizing ultrahigh recoverable energy density and superior charge–discharge performance in $NaNbO_3$-based lead-free ceramics *via* a local random field strategy†

Junpeng Shi, Xiuli Chen,* Xu Li, Jie Sun, Congcong Sun, Feihong Pang and Huanfu Zhou

The development and use of high-performance and environmentally friendly energy storage capacitors are urgently demanded. Despite extensive research efforts, the performance of existing lead-free dielectric ceramics is barely satisfactory. In this work, a novel lead-free $0.78NaNbO_3$–$0.22Bi(Mg_{2/3}Ta_{1/3})O_3$ (0.22BMT) linear-like relaxor ferroelectric with ultrahigh energy storage capability and ultrahigh efficiency was designed and synthesized *via* a local random field strategy. To our satisfaction, an ultrahigh recoverable energy density (W_{rec}, 5.01 J cm^{-3}) and an ultrahigh energy efficiency (η) of 86.1% were achieved simultaneously, which are superior to those of other reported lead-free systems. In addition, excellent temperature, frequency and fatigue stabilities (variation of W_{rec} < 8% over 20–200 °C, W_{rec} < 3% after 1–100 Hz and 10^4 cycles) were observed. More importantly, the 0.22BMT ceramic exhibited a large current density (C_D ~ 537.9 A cm^{-2}), an extremely high power density (P_D ~ 37.7 MW cm^{-3}), and an ultrafast discharge time ($t_{0.9}$ ~ 23 ns). The impedance analysis demonstrated that the introduction of BMT was beneficial for the improvement of the insulation ability and breakdown strength (E_b) of the 0.22BMT ceramic. Additionally, nonisovalent Mg^{2+} and Ta^{5+}-filled Nb^{5+} on the B-site with low average electronegativity generated a random local field, which enhanced the ion bonding, destroyed the long-range order and led to decreased remnant polarization (P_r). These results indicate that this new strategy is a feasible and efficacious means to simultaneously achieve ultrahigh W_{rec}, superior η and excellent thermal stability in NN-based lead-free ceramics. Furthermore, this work has further broadened the scope of research and the application of the NN-based ceramics.

Received 8th December 2019,
Accepted 7th February 2020

DOI: 10.1039/c9tc06711f

rsc.li/materials-c

1. Introduction

With the continuous consumption of non-renewable resources and the increasingly serious environmental problems, the development and utilization of high performance, environmentally friendly energy storage materials have become a research hotspot in current technology and industry.[1–4] With their advantages of light weight, high power density, excellent stability, good environmental adaptability, ageing resistance and low manufacturing cost, dielectric energy storage capacitors show substantial application prospects in automotive electronics, communication, medical equipment and other fields.[5–8] If the energy storage density of the capacitor can be strategically improved, the application field of the capacitor can be further expanded to effectively reduce the volume of the capacitor and achieve the miniaturization and integration of the capacitor. Herein, it is vital to exploit lead-free energy storage ceramic materials with excellent performance and environmental friendliness.[9–15] Generally, there are four kinds of energy storage dielectric: ferroelectrics (FE), relaxor ferroelectrics (RFE), anti-ferroelectrics (AFE) and linear dielectrics (LD). Due to low hysteresis polarization response, the RFE ceramics generally have higher η values; however, the limited W_{rec} values restrict their further applications.[16,17,21] It is hard for anti-ferroelectric materials to bear the long-term cyclic operation because they will probably crack owing to phase transition.[49] By contrast, the LD ceramics have been extensively studied in dielectric capacitors because of their highest E_b and low loss during the discharging process.[18,19] Nevertheless, the W_{rec} of LD is small due to a low relative dielectric constant (ε_r) and small maximum polarization (P_{max}).[21] Based on the above considerations, we focussed on the improvement of E_b, which causes LD to show excellent energy storage performance.[22,23]

Collaborative Innovation Center for Exploration of Hidden Nonferrous Metal Deposits and Development of New Materials in Guangxi, Key Laboratory of Nonferrous Materials and New Processing Technology, Ministry of Education, School of Materials Science and Engineering, Guilin University of Technology, Guilin 541004, China. E-mail: cxlnwpu@163.com

† Electronic supplementary information (ESI) available. See DOI: 10.1039/c9tc06711f

Recently, numerous research results have shown that by B-doping or A- and B- doping, lead-based and lead-free ceramics with excellent energy storage characteristics can be obtained. For example, Zhang *et al.* prepared (Pb, La)(Zr, Ti)O_3 ceramics using the spark plasma sintering method and achieved an ultrahigh W_{rec} of 6.4 J cm^{-3}.[24] Moreover, Han and co-workers also fabricated $(Sm_{0.02}Ag_{0.94})(Nb_{0.9}Ta_{0.1})O_3$ AFE ceramics and obtained a W_{rec} of 4.4 J cm^{-3} at 280 kV cm^{-1}.[25] Li *et al.* found that the W_{rec} values of BT ceramics can be increased to 3 J cm^{-3} and 3.282 J cm^{-3} *via* the addition of $BiMeO_3$ (Me = $Li_{1/3}Zr_{2/3}$, $Mg_{2/3}Ta_{1/3}$) compounds, respectively.[26,27] Lately, a series of dielectric materials with large W_{rec} value were achieved in NN-based ceramics. For instance, Ye *et al.* reported that NN-based ceramics possessed high $W_{rec} \approx 2.8$ J cm^{-3} and $E_b \approx 300$ kV cm^{-1}, benefitting from the intention of enhancing anti-ferroelectricity and constructing a local random field engineered engineering.[57] In addition, both a high W_{rec} of 2.20 J cm^{-3} and η of 62.68% were achieved in $0.91NaNbO_3$–$0.09Bi(Zn_{0.5}Ti_{0.5})O_3$ ceramics at 250 kV cm^{-1} by Fan *et al.*[28] A large W_{rec} of 3.02 J cm^{-3} at 310 kV cm^{-1} for $0.80NaNbO_3$–$0.20SrTiO_3$ ceramics was reported by Zhou *et al.*[20] As mentioned above, lead-based materials are significantly better than lead-free materials in comprehensive energy storage, but the use of numerous lead elements is harmful to the human body. Furthermore, most Ag-based AFE have relatively low η (75%), while Ag oxides are expensive and difficult to prepare.[27] NN-based ceramics can acquire a relatively high W_{rec} and a low η. Specifically, there are few studies reporting that ultrahigh W_{rec} (>5 J cm^{-3}) and η (>80%) can be obtained simultaneously in NN-based or other lead-free systems.

The following strategy was applied in this work. BMT was introduced to control the dielectric properties (*i.e.*, depressing the dielectric nonlinearly, reducing the dielectric loss, and obtaining the appropriate ε_r), which improved the E_b. The significant improvement of energy storage is summarized as follows:

(I) The P_{max} could be strengthened by adjusting the hybridization between the 6p orbital of Bi^{3+} and the 2p orbital of O.[2–27] The larger ionic radii [$(Mg_{2/3}Ta_{1/3})^{3+}$ (0.68 Å) would substitute for $r_{Nb}{}^{5+}$ (0.64 Å)] in the B-site, and greater polarization could encourages larger induced polarization of polar clusters.[28]

(II) The introduction of B-site ions with low polarizability could effectively enhance the antiferroelectricity of NN.[57] Furthermore, nonisovalent Mg^{2+} and Ta^{5+} filled Nb^{5+} on B-site with low average electronegativity generated a random local field, which enhanced the ion bonding, destroyed the long-range order and led to decreased P_r.[28]

(III) The increase of E_b was largely attributed to the compact microstructure, the small grain size, the high-κ insulator such as Ta_2O_5 ($\approx$4 eV) oxide,[23,27] the grain boundary resistivity increase, the interface polarization inhibition, the leakage loss reduction and the inhibition of the expansion of the conductive path.[27]

Based on the above considerations, the energy storage performance of linear-like relaxor ferroelectrics can be conspicuously improved by chemical co-substitution of Bi^{3+} and $(Mg_{2/3}Ta_{1/3})^{3+}$ ions in A and B sites, respectively. As expected, an ultrahigh W_{rec} of 5.01 J cm^{-3} and η of 86.1% of the 0.22BMT ceramic can be achieved, accompanied by excellent temperature, frequency and fatigue stability. Furthermore, the superior stability of η can be observed in the temperature ranging from 20–200 °C, a wide frequency range (1–100 Hz) and fatigue (1–10^4 cycles). More importantly, the 0.22BMT ceramic presents prominent charge–discharge performance with substantial C_D ($\sim$537.9 A cm^{-2}), extremely high P_D ($\sim$37.7 MW cm^{-3}), and ultrafast discharge rate ($\sim$23 ns). These results reveal that the sample could be considered as a promising candidate for lead-free energy storage capacitors.

2. Results and discussion

Fig. 1a displays the XRD patterns of *x*BMT ceramics at room temperature. All the ceramics display the pure perovskite structure without any impurity phase, indicating that BMT is completely diffused into the NN lattice. No splitting of both the (110) and (200) diffraction peaks indicates that the ceramics have a pseudo-cubic phase.[26] The inset of Fig. 1a presents enlarged (110) and (200) diffraction peaks moving towards low angles as the BMT content increases, which may be attributed to volume expansion of the lattice.[27] Generally, Bi^{3+} (1.34 Å, CN = 12) filled Na^+ (1.39 Å, CN = 12) on the A-site while Mg^{2+} (0.72 Å, CN = 6) and Ta^{5+} (0.64 Å, CN = 6) substituted for Nb^{5+} (0.64 Å, CN = 6) on the B-site. Therefore, the increase in the lattice volume (as shown in Fig. 1b) may be due to the substitution of $(Mg_{2/3}Ta_{1/3})^{3+}$ (0.68 Å) for

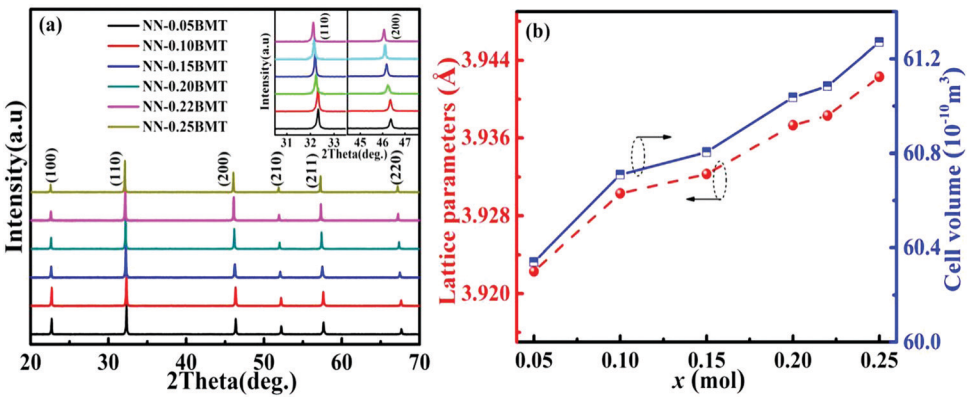

Fig. 1 (a) XRD patterns of BMT-modified NN ceramics. (b) The corresponding Lattice parameters and unit cell volume as a function of *x*.

Nb^{5+} (0.64 Å) on the B-site.[50] Meanwhile, to identify these issues and provide insight into the crystal structure and disorder characteristics of the *x*BMT ceramics, Raman spectroscopy was used, and the results are shown in Fig. S1 (ESI†). The Raman studies manifested that the cation disorder may account for the much slimmer *P*–*E* loops.[8]

To further confirm the detailed phase structure of the 0.22BMT ceramic, a Rietveld refinement was employed *via* the GSAS software and the refined profiles fit the observed data well, as displayed in Fig. 2a. It is remarkable that final refined data and locally enlarged (110) and (200) peaks are observed in the inset of Fig. 2a, indicating that the pseudo-cubic phase is stabilized in the 0.22BMT ceramic. Moreover, the introduction of BMT can markedly decrease the grain size of the *x*BMT compounds, as shown in Fig. 2b and Fig. S2 (ESI†). Fig. 2b exhibits SEM image of the 0.22BMT ceramic, well-developed grains with dense and homogenous microstructure. Specifically, the average grain sizes of the *x*BMT compounds are 5.11, 4.04, 3.77, 2.72, 2.34 and 1.56 μm for $x = 0$, 0.05, 0.10, 0.15, 0.20, and 0.22, respectively. In order to determine the exact composition and the homogeneity of the sintered samples, we performed the elemental mapping analysis of the 0.22BMT ceramics, as shown in Fig. 2c.[29,31] Compared with the initial chemical stoichiometric ratio, the minor compositional variation can be ascribed to both the detection error of the SEM and the element evaporation during sintering. As shown in Fig. S3 (ESI†), the bulk and relative densities of the 0.22BMT ceramics increased to a maximum value of 5.3 g cm^{-3} (98.4%) at a sintering temperature of 1260 °C. A relatively high relative density is desirable for practical applications. This high relative density is satisfactory, as small grain size and dense microstructure are conducive to obtaining ultrahigh E_b.[29] For 0.22BMT ceramics, a similar phenomenon is seen in Fig. 2d. Weibull distribution was adopted to verify the value of E_b of the 0.22BMT ceramic. The reasonable values of E_b can be calculated by the following equations:[25,27]

$$X_i = \ln(E_i), \quad (1)$$

$$Y_i = \ln(\ln(1/(1 - i/(1 + n)))), \quad (2)$$

where E_i, i, and n represent the specific breakdown voltage, the sample sequence and the amount of sample, respectively. E_b and β values of 0.22BMT ceramic are 64.5 kV mm^{-1} and 20.4, respectively. The fitted value of E_b far surpasses other lead-free systems,[25,26] which is beneficial for the energy storage performance of 0.22BMT ceramics.

Fig. 3a manifests the complex impedance spectra of the 0.22BMT ceramic at different temperatures, reflecting the relation between the real part (Z') and the imaginary part (Z'') of impedance. Normally, the grain boundary response is believed to be in the low frequency region. The semicircle in the impedance spectrum is simulated by an equivalent circuit, which shows that the grain boundary response plays a leading role. The movement of the characteristic peak of the grain boundary reflects the change of resistivity in the electron active region.[23] Compared with NN ceramics, the characteristic peak of the 0.22BMT sample moves to

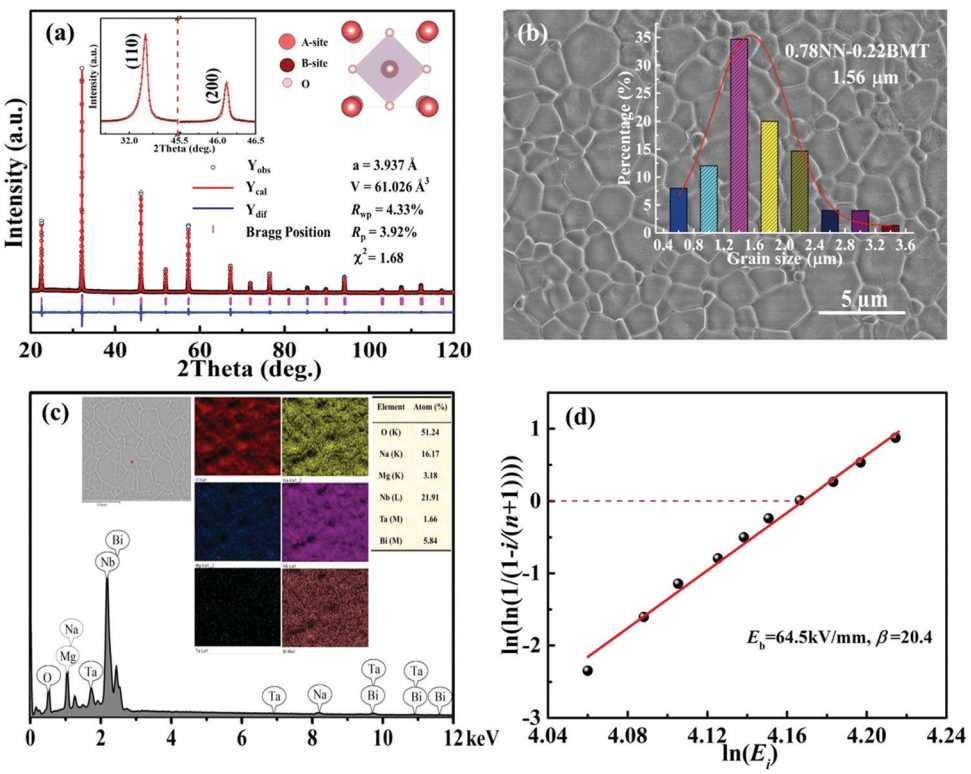

Fig. 2 (a) XRD Rietveld refinement, (b) SEM image, (c) elemental mapping and (d) the Weibull distribution of the E_b for the 0.22BMT ceramic. The inset of (a) shows enlarged (110) and (200) peaks and XRD Rietveld refinement results of the 0.22BMT ceramic. The inset of (b) is a view of the grain size distribution.

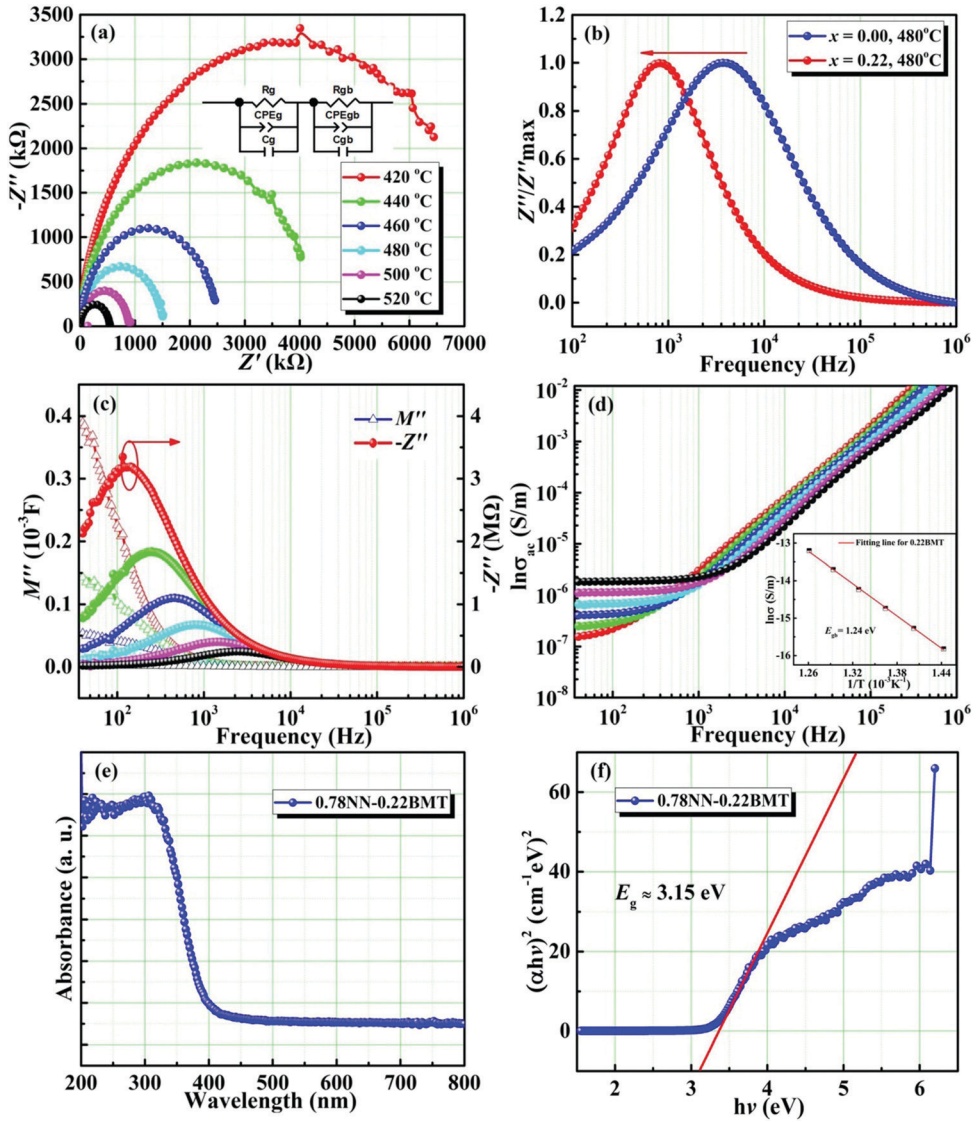

Fig. 3 (a) Impedance spectrum of the 0.22BMT ceramic. (b) The imaginary part of impedance as a function of frequency (at 480 °C) for NN and 0.22BMT ceramics. (c and d) The $-Z''/M''$ spectroscopic plots and frequency dependence of conductivity for 0.22BMT ceramic. (e and f) Energy dependence of $(\alpha h\nu)^2$ for 0.22BMT sample.

a lower frequency, which means that the resistivity increases due to the introduction of BMT. As shown in Fig. 3b, the imaginary part of impedance at different temperatures and frequencies has only one characteristic peak, which is consistent with the complex impedance spectrum. To further determine that the semicircle (Fig. 3a) reflects the role of the grain boundary, the modulus spectrum is introduced for further analysis in Fig. 3c. The impedance spectrum reflects the resistance characteristics of the material, and the modulus spectrum more clearly reflects the contribution of the different parts of the capacitance. The conversion relationship between the electronic modulus (M) and the impedance (Z) is as follows:[33]

$$M = i\omega C_0 Z = M' - iM'', \tag{3}$$

$$M'' = \frac{C_0}{C}\frac{\omega RC}{1+(\omega RC)^2}, \tag{4}$$

where $C_0 = \omega_0 S/d$ is the vacuum capacitance, ω_0 is the vacuum permittivity, and S and d are the area and thickness of the sample, respectively. The analysis of the impedance spectrum and the modulus spectrum demonstrates that the grain boundary of the 0.22BMT ceramic plays a dominant role in the electrical properties of the materials. Fig. 3d displays the frequency dependence of conductivity of the 0.22BMT ceramics ranging from 420 °C to 520 °C. There is a conductive platform in the low frequency region, and its conductivity value is related to the DC conduction behaviour. Especially, the conductivity of the BMT-doped samples decreased significantly in the test range. To further identify the effect of the addition of BMT on the conductivity of the 0.22BMT ceramics, the activation energy of the grain boundary (E_{gb}) will be determined in the following equation:[23]

$$\sigma_{gb} = \sigma_0 \exp\left(\frac{E_{gb}}{k_B T}\right), \tag{5}$$

where σ_0 is the constant and k_B is the Boltzmann constant. The relationship between the conductivity and temperature is shown in the inset of Fig. 3d. According to the slope of the $\ln\sigma$ *vs.* $1/T$ curve, the activation energy E_{gb} is 1.53 eV.

To verify the effect of the band gap on improving E_b, the investigation of band gap energy (E_g) is shown in Fig. 3e and f. The band gap energy can be given as follows:[22,32]

$$(\alpha h\nu)^{1/n} = A(h\nu - E_g), \quad (6)$$

where A, $h\nu$ and n are the constant, incident photon energy and types of electronic transitions, respectively. The E_g can be obtained by extrapolating the linear part of the ordinate value of Fig. 3e and f, which is represented as the intercept of the line when the ordinate is 0. Furthermore, the intersection of the abscissa is the approximate value of E_g of the 0.22BMT ceramic, which is estimated to be approximately 3.15 eV. Therefore, the 0.22BMT ceramic has a wider E_g. Generally, NN-based ceramics should have a higher intrinsic E_b to achieve large superiority in energy storage capacitors, as proved in Fig. 2d.[20–23]

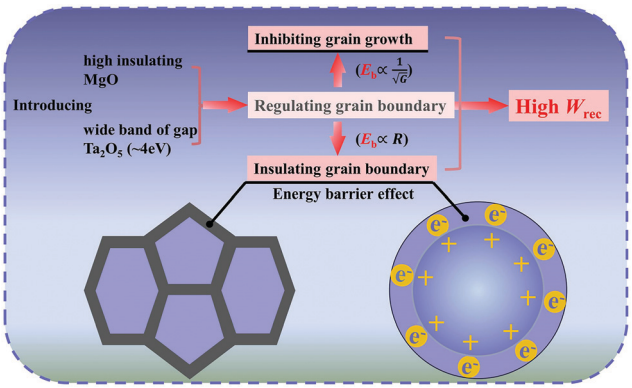

Fig. 4 The mechanism of obtaining excellent energy storage properties.

Based on the aforementioned discussions, the schematic diagram of excellent energy storage properties is shown in Fig. 4. The mechanism is associated with the moderate ε_r, insulating resistance grain boundaries and inhibiting grain growth. The ultrahigh E_b can be explained by the mechanism. Due to the high insulation, the grain boundary usually acts as an impediment to conduction. Smaller grain size means higher grain boundary density. The grain boundary can effectively block the charge migration under the external electric field. As a result, electrons will move smoothly in the grains but amass at the grain boundaries.[34] The introduction of BMT has the advantage of improving the insulation resistance grain boundary and grain boundary barrier effect, which is conducive to achieving an ultrahigh E_b and improving energy storage performance.

Fig. 5a demonstrates the relationship between the dielectric properties and temperature of 0.22BMT ceramics under different frequencies. The ceramics exhibit a proper ε_r and remain stable with the increasing the frequency, as shown in Fig. 5a. A weakly relaxor behavior was observed and verified due to the dielectric peak corresponding to frequency dispersion,[40–43] which can be attributed to the substitution of Bi^{3+} at the A-site and the occupancy of Mg^{2+} and Ta^{5+} at the B-site. In addition, Fig. 5b demonstrates that the change in ε_r with temperature is effectively

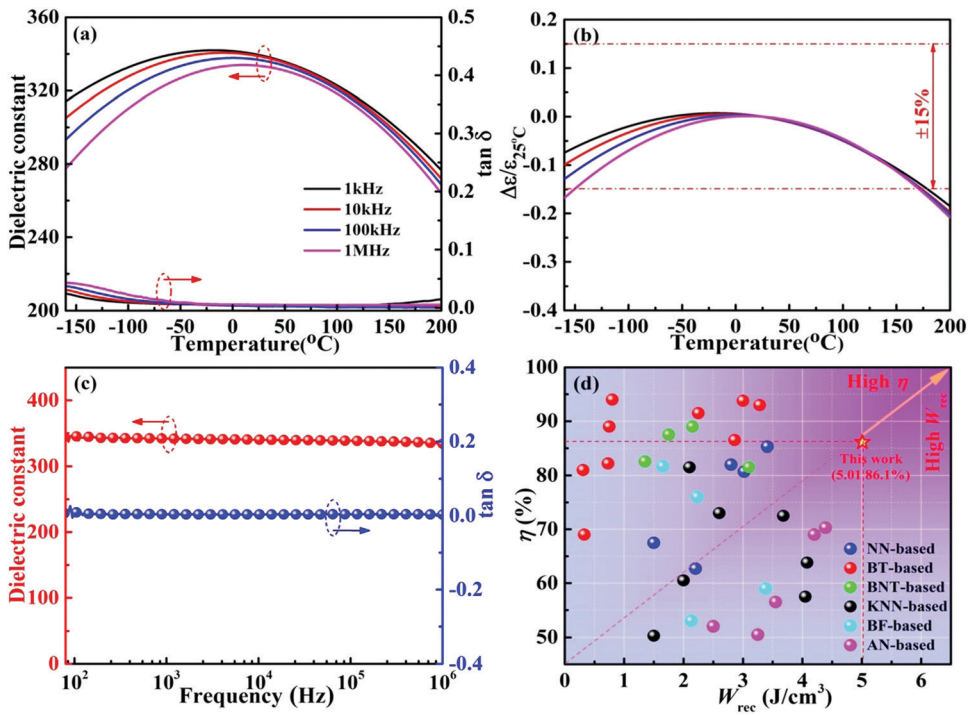

Fig. 5 (a) Temperature dependence of the dielectric constant and loss of the 0.22BMT ceramic. (b) Temperature coefficient of permittivity as a function of temperature at different frequencies from 1 kHz to 1 MHz for the 0.22BMT ceramic. (c) Frequency dependence of dielectric constant and dielectric loss for the 0.22BMT ceramic at room temperature. (d) The comparison of W_{rec} and η for lead-free ceramics.

suppressed, especially for the dielectric constant $\Delta\varepsilon/\varepsilon_{25\,^{\circ}C} \leq \pm 15\%$ (T = −160–180 °C) and low loss tangent $\tan\delta < 3\%$ (T = −160–200 °C) of the 0.22BMT ceramic exhibiting excellent temperature stability and application prospects of high temperature capacitor X8R.[27,36] Fig. 5c depicts the function of frequency and temperature. The ε_r and $\tan\delta$ almost remain at the same level in the testing frequency range. The dielectric properties exhibit good frequency stability, which is conducive to energy storage in the energy storage capacitors. The above conclusions are related to the high E_b and high polarization obtained. Larger dielectric constant and ultralow loss are beneficial for enhancing E_b. Fig. 5d summarizes the W_{rec} and η [6,8–12,14,28–39,44–59] between this work and other recently reported lead-free bulk ceramics. For example, medium W_{rec} and η are exhibited by $BiFeO_3$-based and BNT-based ceramics. $BaTiO_3$-based ceramics show relatively low W_{rec} and high η values, while the opposite trend is shown in $AgNbO_3$-based and $(K_{0.5}Na_{0.5})NbO_3$-based systems. In particular, it can be seen from the Fig. 5d that an ultrahigh W_{rec} and η are realized simultaneously in the 0.22BMT ceramic, which are almost obviously superior to most of the other lead-free bulk ceramics reported in the literature. In addition, the 0.22BMT ceramic exhibits outstanding comprehensive properties and has a broad prospect in the practical application of capacitors.

Fig. 6(a) displays the unipolar P–E loops of xBMT ceramics measured at 10 Hz under E_b. As the x-content increases, the unipolar P–E loops increase linearly, accompanied by a gradually decrease in P_r. Upon increasing the BMT content from 0.05 to 0.25, the xBMT ceramic gradually changes from relaxor AFEs to linear dielectrics, which is conducive to obtaining excellent W_{rec} and η. As shown in Fig. 6b, both P_{max} and P_r gradually decrease, accompanied by a low P_{max}–P_r ($\leq$1.4 μC cm^{-2}) in the 0.22BMT ceramic. Fig. 6c and d show the energy storage performances of xBMT ceramics. The values of W_{rec} and η significantly increase from 2.1 J cm^{-3} and 55% to 5.01 J cm^{-3} and 86.1%, respectively, upon increasing the BMT content from x = 0.05 to x = 0.22. Simultaneously achieving an ultrahigh W_{rec} and η in the 0.22BMT ceramic may be attributed to the highest E_b. Consequently, by introducing BMT into the NN solution, its energy storage performance is greatly enhanced.

To further understand the excellent energy storage performance of the 0.22BMT ceramic, the unipolar P–E curves are shown in Fig. 7. With the increase of the electric field, the slender P–E loops gradually extend outward in Fig. 7a. The 0.22BMT ceramics sample presents ultraslim P–E loops and smaller P_r, which indicate that the ceramics will need less energy loss during the charge and discharge processes, showing that the 0.22BMT ceramic exhibit high efficiency of $\geq$ 86.1%. Meanwhile, the larger E_b is clearly presented in Fig. 7b and is due to the wide band gap of high-κ insulator Ta_2O_5 ($\sim$4 eV). The 0.22BMT ceramic has a wider Eg, and the electrons in the valence band do not easily jump into the conduction band, which would contribute to a high possibility of intrinsic breakdown.[27] A convenient path for the charge transfer is between grains and grain boundaries, leading to a transition from the charge localization state to the charge diffusion state, which accounts for depressed interfacial polarization. It can be obtained that

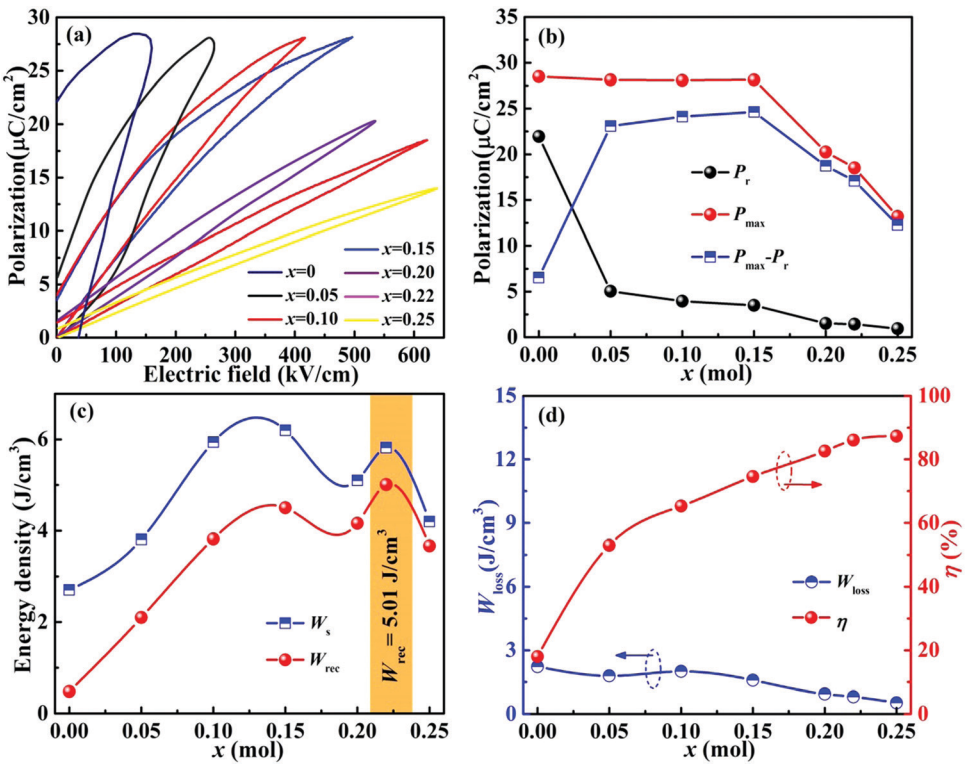

Fig. 6 (a) Unipolar P–E loops for xBMT ceramics at E_b. (b) Variation of P_{max} and P_r as a function of x content. (c) W_s and W_{rec}, and (d) W_{loss} and η *versus* applied electric field of various xBMT ceramics.

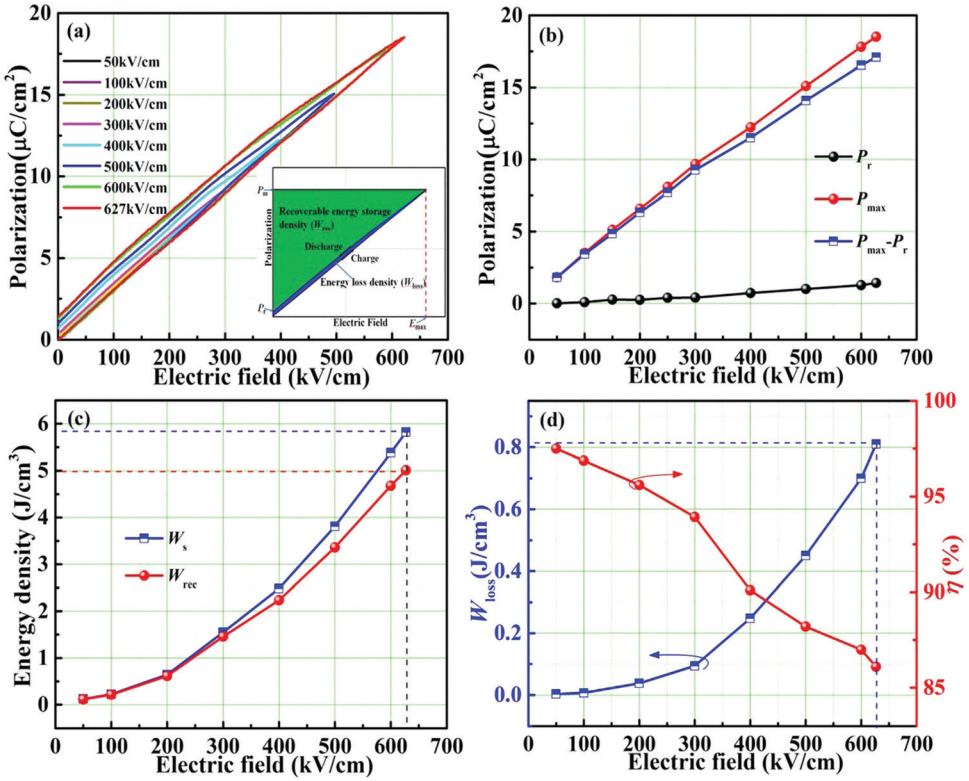

Fig. 7 Unipolar *P*–*E* loops and energy storage properties of the 0.22BMT ceramic varied with different electric fields.

with the increase of the applied electric field, the value of P_{max} displays a prominent enhancement from 1.822 to 18.512 μC cm^{-2}, while the change in P_r remains very small (0.014–1.423 μC cm^{-2}). Fig. 7c and d depicts a somewhat stable relationship among W_{rec}, η and the electric field, which meets the application requirements. The increase of W_{rec} may be attributed to the increase of E_b, as confirmed by the dielectric and the impedance spectra (Fig. 4 and 5). As expected, ultrahigh W_{rec} (5.01 J cm^{-3}), E_b (627 kV cm^{-1}) and η (86.1%) in the 0.22BMT ceramic are simultaneously achieved.

For practical applications, the stability of the frequency, temperature and fatigue is one of significant parameters for designing the energy storage capacitors. Fig. 8a demonstrates the unipolar *P*–*E* loops of the 0.22BMT ceramic from 1 to 100 Hz under 380 kV cm^{-1}. Obviously, the very slender *P*–*E* loops illustrate that the 0.22BMT ceramic exhibits a typical linear-like relaxor ferroelectric characteristic over the wide frequency range. Fig. 8b shows that the values of W_{rec} range from 2.30 to 2.24 J cm^{-3} (*i.e.*, a variation of W_{rec} < 3%) and all the corresponding η values remain above 93%. Furthermore, the stability of the frequency may be attributed to the compact microstructure of the ceramic. Fig. 8c displays the W_{rec} and η values as a function of different temperatures. In particular, the values of W_{rec} and η vary from 2.29 J cm^{-3} and 95.14% to 2.11 J cm^{-3} and 91.47% when the temperature increases from 20 °C to 200 °C, *i.e.*, the variation is less than 8% and 4%, respectively (Fig. 8d). Moreover, the *P*–*E* loops always remain ultraslim, which may be owing to the lower P_r values in the temperature range of 20–200 °C. However, the *P*–*E* loops of the 0.22BMT ceramic change slightly with increasing temperatures, which may be due to the activation heat movement of carriers on oxygen vacancies (see Fig. S4, ESI†), leading to the rise of ionic conduction and leakage loss.[23] Excellent antifatigue performance is another indispensable condition for the practical application of ceramic capacitors. Fig. 8e shows the fatigue cycles dependence of the *P*–*E* loops of the 0.22BMT ceramic. No notable change in the *P*–*E* loops in the range of 10^{-1}–10^4 cycles was obtained. The values of P_{max} and P_r values were stable at approximately 11.87 μC cm^{-2} and 0.30 μC cm^{-2} respectively (the inset of Fig. 8e). The dependence of the fatigue cycles on W_{rec} and η is shown in Fig. 8f. The ceramic exhibited excellent fatigue stability even after 10^4 fatigue cycles, with only a slight change in ΔW_{rec} < 3% and $\Delta\eta$ < 1%. All these factors are expected to increase the comprehensive energy storage properties.

Fig. 9(a) presents the curves between the underdamped discharge electric current and time for 0.22BMT ceramics at room temperature and under the various values of *E*. Interestingly, the 0.22BMT ceramics exhibit the same discharging behaviours at different electric fields, and the first current peak increases linearly with the increase in the electric field strength. Fig. 9(b) displays the variation of current peak (I_{max}), current density ($C_D = I_{max}/S$), and power density ($P_D = EI_{max}/2S$; *S*: electrode area) of as functions of the electric field. The I_{max} shows a significant increment (from 6.3 A to 38 A). Meanwhile, the corresponding C_D and P_D reached the top value of 537.9 A cm^{-2} and 37.7 MW cm^{-3} respectively at the maximum electric field of 14 kV mm^{-1}. Fig. 9(c) exhibits the temperature dependence of the stored charge and energy release

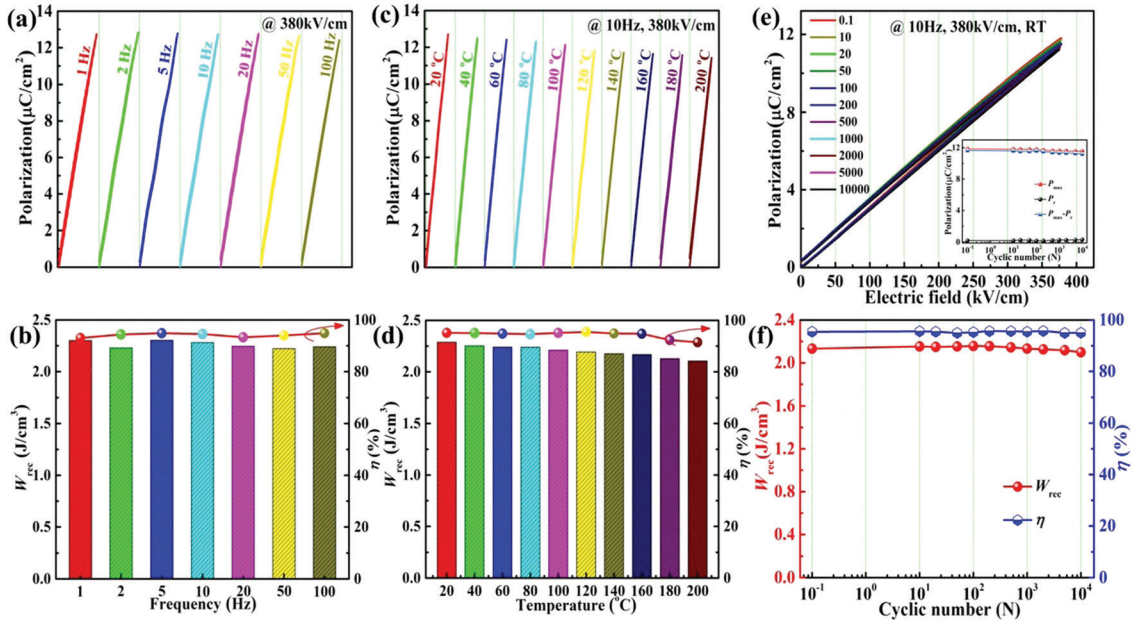

Fig. 8 Unipolar *P*–*E* hysteresis loops (a and c) and the corresponding energy storage properties (b and d) for 0.22BMT ceramics at different frequencies and temperatures under different electric fields. The cycle number dependence of (e) unipolar *P*–*E* loops and (f) energy storage properties of 0.22BMT ceramics.

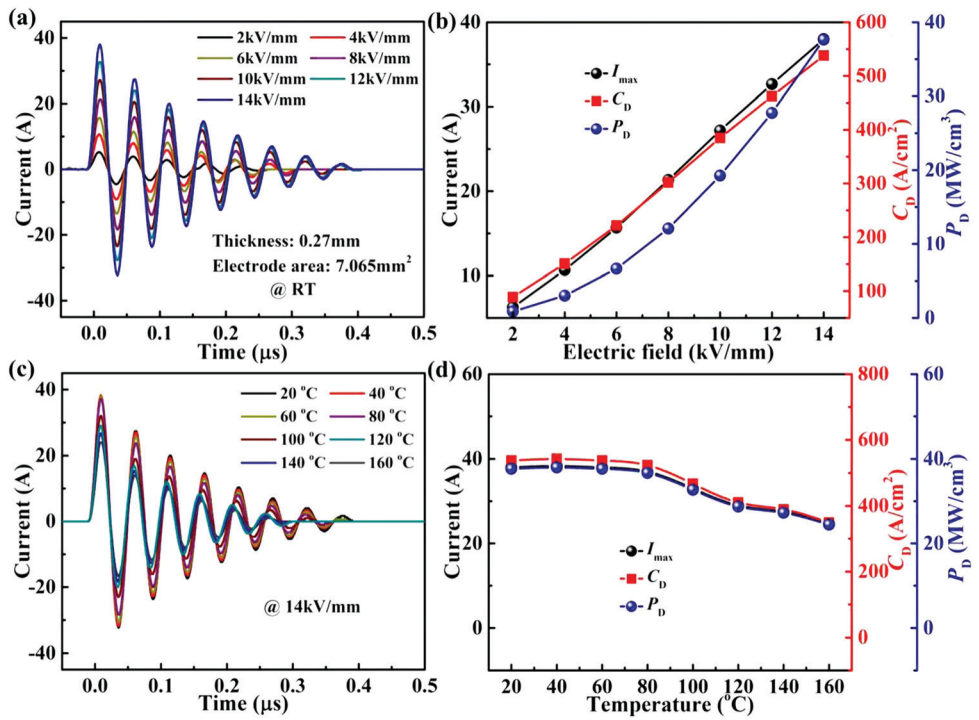

Fig. 9 (a) Underdamped discharge waveforms of the 0.22BMT ceramics under various electric fields and room temperature. (b) Variations of I_{max}, C_D, and P_D as functions of the applied electric field. (c) Underdamped discharge waveforms of the 0.22BMT ceramics at different temperatures under 14 kV mm^{-1}. (d) Variations of I_{max}, C_D, and P_D as functions of the temperature.

performances at a fixed electric field (14 kV mm^{-1}). The stored charge is observed to be released more rapidly ($\leq$0.4 μs) with the increasing temperature at various electric field strengths. The first I_{max} shows a slight decrement (from 38 A to 24.7 A) when the temperature rises from 20 °C to 160 °C. The thermal stability of 0.22BMT ceramics reaches a steady-state value from 20 to 100 °C, and when the temperature increases further, the values of C_D and P_D decrease from 467.1 A cm^{-2} and 32.7 MW cm^{-3} to 349.1 A cm^{-2} and 24.4 MW cm^{-3}. The variations of I_{max}, C_D, and P_D are less than ±15% over 20–160 °C.

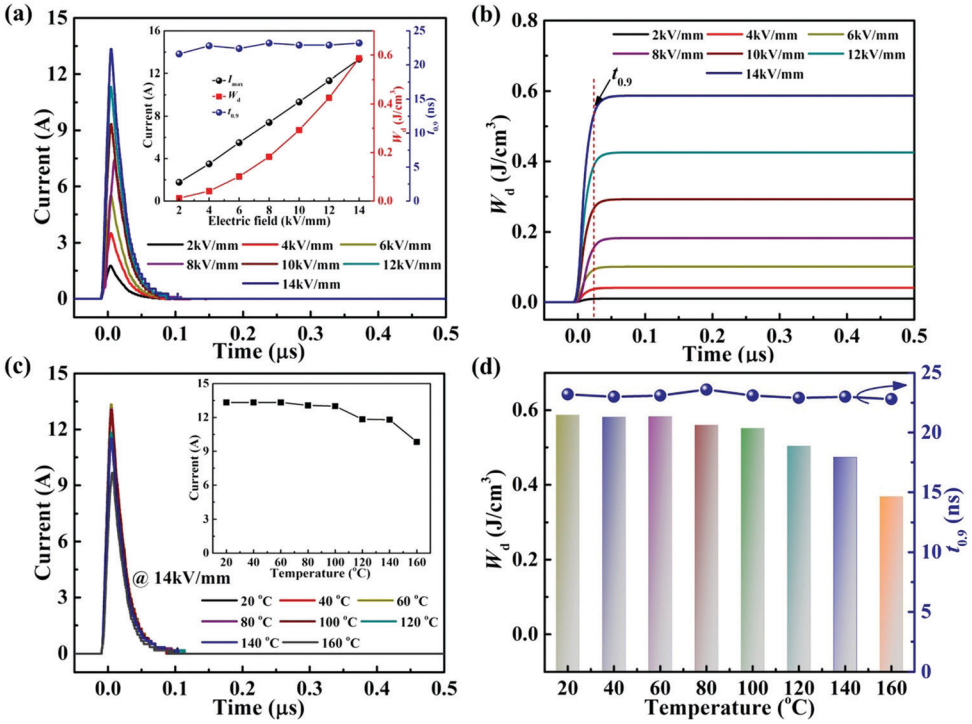

Fig. 10 (a) Overdamped discharge current curves of the 0.22BMT ceramics at different electric fields; the inset displays the variations of current peak, W_d and $t_{0.9}$ as functions of the electric field. (b) Electric-field dependence of the relationship between W_d and time. (c) Overdamped discharge waveforms of the 0.22BMT ceramics at different temperatures under 14 kV mm^{-1}. (d) Variation of W_d and $t_{0.9}$ as functions of temperature. Fluctuations of W_d and $t_{0.9}$ as functions of the temperature.

The time dependence of the discharged energy density (W_d) is calculated as: $W_d = R\int i^2(t)dt/V$,[26] where R is the load resistor, and V is sample volume. The $t_{0.9}$ indicates the time needed to release 90% of the stored energy. The effect of the electric field on the pulsed-discharge performance of the 0.22BMT ceramics at a fixed load resistance of 202.5 Ω is given in Fig. 10a. The inset of Fig. 10a depicts the electric field dependence of $t_{0.9}$, I_{max}, and W_d, which displays that the value of $t_{0.9}$ remains stable and ultrafast time (~23 ns) over a wide range of 2–14 kV mm^{-1}. In addition, the I_{max} and W_d values depend on the electric field, increasing from 1.8 A and 0.012 J cm^{-3} at 2 kV mm^{-1} to 13.3 A and 0.587 J cm^{-3} at 14 kV mm^{-1}. The overdamped discharge current waveforms of the 0.22BMT ceramics and the corresponding $t_{0.9}$, I_{max}, and W_d in the temperature range of 20 °C to 160 °C at 14 kV mm^{-1} (as displayed in Fig. 10c and d). Remarkably, a temperature-induced $t_{0.9}$ (~23 ns, @ 14 kV mm^{-1}) varying within less than 2% in the temperature range of 20–160 °C was found in the 0.22BMT ceramics. As a consequence, the charge–discharge properties ($W_d \geq 0.56$ J cm^{-3}, $I_{max} \geq 13$ A, and $t_{0.9} \leq 23$ ns) of the 0.22BMT ceramics from 20 °C to 100 °C under an electric field of 14 kV mm^{-1} are desirable for pulsed power capacitor applications. A comparison of the charge–discharge properties of many energy storage ceramics is summarized in Table S1 (ESI†). Although lead-based energy storage ceramics were reported to have an ultrahigh W_{rec} value, its $t_{0.9}$ value is relatively low. Obviously, the 0.22BMT system possesses a very short and stable $t_{0.9}$, which is superior to most bulk energy storage ceramics.

3. Conclusions

In summary, we constructed a local random field strategy to enhance the W_{rec} of lead-free ceramics. A novel 0.22BMT solid solution was rationally designed for achieving a large P_{max}, and ultrahigh W_{rec} and η. As expected, an ultrahigh W_{rec} (~5.01 J cm^{-3}) and η (~ 86.1%) were achieved in the 0.22BMT ceramics. Furthermore, with the increasing frequency (1–100 Hz) and temperature (20–200 °C), the energy storage properties of the 0.22BMT ceramic demonstrate its excellent thermal stability. In addition, the ceramic exhibited excellent fatigue stability even after 10^4 fatigue cycles, with only a slight change in $\Delta W_{rec} < 3\%$ and $\Delta\eta < 1\%$. The 0.22BMT ceramic presents prominent charge–discharge performance with large C_D (~537.9 A cm^{-2}), extremely high P_D (~37.7 MW cm^{-3}), and ultrafast discharge rate (~23 ns). This work provides a novel avenue for the design of high energy storage lead-free dielectric materials and broadens the applications field for NN-based ceramics.

4. Experimental procedure

The experimental processes for xBMT ceramics are briefed in the supporting material.

Conflicts of interest

There are no conflicts to declare.

Acknowledgements

This work was supported by National Natural Science Foundation of China (No. 11664008 and 61761015), Natural Science Foundation of Guangxi (No. 2018GXNSFFA050001, 2017GXNSFDA198027 and 2017GXNSFFA198011).

References

1 L. Yang, X. Kong, F. Li, H. Hao, Z. Cheng, H. Liu, J. F. Li and S. Zhang, *Prog. Mater. Sci.*, 2019, **102**, 72–108.
2 S. Kwon and W. Hackenberger, *IEEE Electr. Insul. Mag.*, 2011, **27**, 43–55.
3 Z. Yao, Z. Song, H. Hao, Z. Yu, M. Cao, S. Zhang, M. T. Lanagan and H. Liu, *Adv. Mater.*, 2017, **29**, 1601727.
4 Z. Liu, T. Lu, J. Ye, G. Wang, X. Dong, R. Withers and Y. Liu, *Adv. Mater. Sci. Technol.*, 2018, **3**, 1800111.
5 O. Ellabban, H. Abu-Rub and F. Blaabjerg, *Renewable Sustainable Energy Rev.*, 2014, **39**, 748–764.
6 N. Luo, K. Han, F. Zhuo, L. Liu, X. Chen, B. Peng, X. Wang, Q. Feng and Y. Wei, *J. Mater. Chem. C*, 2019, **7**, 4999–5008.
7 N. Wei, L. H. Yu, Z. T. Sun, Y. Z. Song, M. L. Wang, Z. N. Tian, Y. Xia, J. S. Cai, Y. Y. Li and L. Zhao,, *ACS Nano*, 2019, **13**, 7517–7526.
8 X. Chen, X. Li, H. Zhou, J. Sun, X. Li, X. Yan, C. Sun, J. Shi and F. Pang, *J. Mater. Sci.: Mater. Electron.*, 2019, **30**, 15912–15922.
9 J. Yin, Y. Zhang, X. Lv and J. Wu, *J. Mater. Chem. A*, 2018, **6**, 9823–9832.
10 Z. B. Pan, L. M. Yao, J. W. Zhai, K. Yang, B. Shen and H. T. Wang, *ACS Sustainable Chem. Eng.*, 2017, **5**, 4707–4717.
11 Y. H. Huang, Y. J. Wu, W. J. Qiu, J. Li and X. M. Chen, *J. Eur. Ceram. Soc.*, 2015, **35**, 1469–1476.
12 M. X. Zhou, R. H. Liang, Z. Y. Zhou and X. L. Dong, *Inorg. Chem. Front.*, 2019, **6**, 2148–2157.
13 N. Sun, Y. Li, Q. Zhang and X. Hao, *J. Mater. Chem. C*, 2018, **6**, 40.
14 K. Bi, M. H. Bi, Y. N. Hao, W. Luo, Z. M. Cai, X. H. Wang and Y. H. Huang, *Nano Energy*, 2018, **51**, 513–523.
15 Z. M. Dang, J. K. Yuan, S. H. Yao and R. J. Liao, *Adv. Mater.*, 2013, **25**, 6334–6365.
16 X. Dong, H. Chen, M. Wei, K. Wu and J. Zhang, *J. Alloys Compd.*, 2018, **744**, 721–727.
17 J. Gao, Y. Zhang, L. Zhao, K. Y. Lee, Q. Liu, A. Studer, M. Hinterstein, S. Zhang and J. F. Li, *J. Mater. Chem. A*, 2019, **7**, 2225–2232.
18 M. Sharifzadeh Mirshekarloo, K. Yao and T. Sritharan, *Appl. Phys. Lett.*, 2010, **97**, 142902.
19 Y. Tian, L. Jin, H. Zhang, Z. Xu, X. Wei, G. Viola, I. Abrahams and H. Yan, *J. Mater. Chem. A*, 2017, **5**, 17525–17531.
20 M. X. Zhou, R. H. Liang, Z. Y. Zhou, S. G. Yan and X. L. Dong, *ACS Sustainable Chem. Eng.*, 2018, **6**, 12755–12765.
21 H. Qi and R. Zuo, *J. Mater. Chem. A*, 2019, **7**, 3971–3978.
22 W. Wang, Y. P. Pu, X. Guo, R. K. Shi, Y. Shi, M. D. Yang, J. W. Li, X. Peng and Y. Li, *J. Eur. Ceram. Soc.*, 2019, **39**, 5236–5242.
23 W. Wang, Y. P. Pu, X. Guo, T. Ouyang, Y. Shi, M. D. Yang, J. W. Li, R. K. Shi and G. Liu, *Ceram. Int.*, 2019, **45**, 14684–14690.
24 Q. F. Zhang, Y. Dan, J. Chen, Y. M. Lu, T. Q. Yang, X. Yao and B. Y. He, *Ceram. Int.*, 2017, **43**, 11428–11432.
25 K. Han, N. N. Luo, S. F. Mao, F. P. Zhuo, L. J. Liu, B. L. Peng, X. Y. Chen, C. Z. Hu, H. F. Zhou and Y. Z. Wei, *J. Mater. Chem. A*, 2019, **7**, 26293–26301.
26 X. Li, X. Chen, J. Sun, M. X. Zhou and H. F. Zhou, *Ceram. Int.*, 2020, **46**, 3426–3432.
27 X. L. Chen, X. Li, J. Sun, C. C. Sun, J. P. Shi, F. H. Pang and H. F. Zhou, *Ceram. Int.*, 2020, **46**, 2764–2771.
28 Y. Z. Fan, Z. Y. Zhou, R. H. Liang and X. L. Dong, *J. Eur. Ceram. Soc.*, 2019, **39**, 4770–4777.
29 M. Zhou, R. Liang, Z. Zhou and X. Dong, *J. Mater. Chem. C*, 2018, **6**, 8528–8537.
30 W. B. Li, D. Zhou, L. X. Pang, R. Xu and H. H. Guo, *J. Mater. Chem. A*, 2017, **5**, 19607–19612.
31 Q. Yuan, G. Li, F. Z. Yao, S. D. Cheng, Y. Wang, R. Ma, S. B. Mi, M. Gu, K. Wang, J. F. Li and H. Wang, *Nano Energy*, 2018, **52**, 203–210.
32 E. K. Abdel-Khalek, I. Ibrahim, T. M. Salama, A. M. Elseman and M. M. Mohamed, *J. Magn. Magn. Mater.*, 2018, **465**, 309–315.
33 Y. Lin, D. Li, M. Mang, S. L. Zhan, Y. D. Yang, H. B. Yang and Q. B. Yuan, *ACS Appl. Mater. Interfaces*, 2019, **11**, 36824–36830.
34 G. C. Liu, H. Q. Fan, J. Xu, Z. Y. Liu and Y. W. Zhao, *RSC Adv.*, 2016, **6**, 48708–48714.
35 M. Zhou, R. Liang, Z. Zhou and X. Dong, *J. Mater. Chem. C*, 2018, **6**, 8528–8537.
36 J. P. Shi, Y. J. Yu, X. L. Chen, G. F. Liu, X. Y. Jiang, J. L. Liang, J. J. Ling, M. Z. Xu and H. F. Zhou, *Appl. Phys. A: Mater. Sci. Process.*, 2019, **125**, 608.
37 (*a*) Q. Yuan, G. Li, F.-Z. Yao, S.-D. Cheng, Y. Wang, R. Ma, S.-B. Mi, M. Gu, K. Wang, J. F. Li and H. Wang, *Nano Energy*, 2018, **52**, 203–210; (*b*) Z. Yang, F. Gao, H. Du, L. Jin, L. Yan, Q. Hu, Y. Yu, S. Qu, X. Wei, Z. Xu and Y. J. Wang, *Nano Energy*, 2019, **58**, 768–777.
38 Z. T. Yang, H. L. Du, S. B. Qu, Y. D. Hou, H. Ma, J. F. Wang, J. Wang, X. Y. Wei and Z. Xu, *J. Mater. Chem. A*, 2016, **4**, 13778–13785.
39 H. Qi and R. Zuo, *J. Mater. Chem. A*, 2019, **7**, 3971–3978.
40 X. Chen, J. Chen, D. Ma, L. Fang and H. Zhou, *Ceram. Int.*, 2015, **41**, 2081–2088.
41 X. Chen, X. Li, H. Zhou, J. Sun, X. Li, X. Yan, C. Sun and J. Shi, *J. Adv. Ceram.*, 2019, **8**, 427–437.
42 X. Chen, X. Li, X. Yan, G. Liu and H. Zhou, *J. Electron. Mater.*, 2018, **47**, 2576–2583.
43 J. Chen, X. Chen, F. He, Y. Wang, H. Zhou and L. Fang, *J. Electron. Mater.*, 2014, **43**, 1112–1118.
44 M. Zhou, R. Liang, Z. Zhou and X. Dong, *Ceram. Int.*, 2019, **45**, 3582–3590.
45 L. Zhang, Y. Pu and M. Chen, *J. Alloys Compd.*, 2019, **775**, 342–347.
46 Y. Yang, H. Wang, L. Bi, Q. Zheng, G. Fan, W. Jie and D. Lin, *J. Eur. Ceram. Soc.*, 2019, **39**, 3051–3056.

47 J. Wu, A. Mahajan, L. Riekehr, H. Zhang, B. Yang, N. Meng, Z. Zhang and H. Yan, *Nano Energy*, 2018, **50**, 723–732.
48 Y. Wu, Y. Fan, N. Liu, P. Peng, M. Zhou, S. Yan, F. Cao, X. Dong and G. Wang, *J. Mater. Chem. C*, 2019, **7**, 6222–6230.
49 T. Shao, H. Du, H. Ma, S. Qu, J. Wang, J. Wang, X. Wei and Z. Xu, *J. Mater. Chem. A*, 2017, **5**, 554–563.
50 B. Y. Qu, H. L. Du and Z. T. Yang, *J. Mater. Chem. C*, 2016, **4**, 1795–1803.
51 X. L. Gao, Y. Li, J. W. Chen, C. Yuan, M. Zeng, A. H. Zhang, X. S. Gao, X. B. Lu, Q. L. Li and J. M. Liu, *J. Eur. Ceram. Soc.*, 2019, **39**, 2331–2338.
52 D. Wang, Z. Fan, W. Li, D. Zhou, A. Feteira, G. Wang, S. Murakami, S. Sun, Q. Zhao, X. Tan and I. M. Reaney, *ACS Appl. Energy Mater.*, 2018, **1**, 4403–4412.
53 D. G. Zheng and R. Z. Zuo, *J. Eur. Ceram. Soc.*, 2017, **37**, 413–418.
54 H. G. Yang, H. Qi and R. Z. Zuo, *J. Eur. Ceram. Soc.*, 2019, **39**, 2673–2679.
55 L. Zhao, J. Gao, Q. Liu, S. Zhang and J. F. Li, *ACS Appl. Mater. Interfaces*, 2018, **10**, 819–826.
56 L. Zhao, Q. Liu, S. Zhang and J. F. Li, *J. Mater. Chem. C*, 2016, **4**, 8380–8384.
57 J. Ye, G. Wang, M. Zhou, N. Liu, X. Chen, S. Li, F. Cao and X. Dong, *J. Mater. Chem. C*, 2019, **7**, 5639–5645.
58 M. X. Zhou, R. H. Liang, Z. Y. Zhou and X. L. Dong, *J. Mater. Chem. A*, 2018, **6**, 17896–17904.
59 Z. Yang, H. Du, L. Jin, Q. Hu, S. Qu, Z. Yang, Y. Yu, X. Wei and Z. Xu, *J. Eur. Ceram. Soc.*, 2019, **39**, 2899–2907.